Electrochimica Acta 427 (2022) 140902

Contents lists available at ScienceDirect

Electrochimica Acta

journal homepage: www.journals.elsevier.com/electrochimica-acta

Predicting optimal geometries of 3D-printed solid oxide electrochemical reactors

I. Jang *, J.C. Alexander, N.M. Farandos, G.H. Kelsall

Department of Chemical Engineering, Imperial College London, London SW7 2AZ, UK

ARTICLE INFO

Keywords:
Solid oxide fuel cells (SOFCs)
Solid oxide electrolysers (SOEs)
3D printing
Finite element modelling

ABSTRACT

Solid oxide electrochemical reactors (SOERs) may be operated in fuel cell (SOFC) or electrolyser (SOE) modes, at temperatures > 800 K, depending on electrolyte and electrode materials. In electrolyser mode, current densities of ≥ ca. 10^4 A m^{-2} are achievable at potential differences ideally at the thermoneutral values of 1.285 V for steam splitting or 1.46 V for CO_2 splitting at 750 °C. As for large scale chemical processes in general, such reactors are required to be energy efficient, economic, of scalable design and fabrication, and durable ideally over ≥ ca. 10 years.

Increasing densities of electrode | electrolyte interfacial areas (and electrode | electrolyte | pore triple phase boundaries) of solid oxide fuel cells or electrolysers offers one means of increasing performance, reproducibility, durability and potentially decreasing cost. Three-dimensional structuring of those interfaces can be achieved by 3D printing, but modelling is required to optimise geometries. Using kinetic parameter values from the literature, COMSOL Multiphysics® finite element software was used to predict effects of 3D geometries, increasing interfacial to geometric area ratios, on SOER performances for YSZ ($(ZrO_2)_{0.92}(Y_2O_3)_{0.08}$) oxide ion conducting electrolyte and Ni-YSZ electrode based cells, relative to corresponding planar structures with < 10 μm thick planar YSZ electrolyte. For the negative electrode, electrolyte and electrode layers were inkjet printed on Ni(O)-YSZ substrate precursors, then sintered. For the positive electrode, porous lanthanum strontium manganite (LSM: $La_{0.8}Sr_{0.2}MnO_{3-\delta}$) was brush-coated over the (gas-tight) YSZ, then sintered to produce complete SOERs: H_2O-H_2 | Ni(O)-YSZ | YSZ-YSZ pillars | YSZ-LSM | LSM | O_2.

Results are reported showing that, in the case of solid YSZ pillars, despite interfacial electrode | electrolyte areas being up scaled by factors of 10–150 depending on height (10–150 μm), current densities were predicted to increase by only ca. 1.14 in electrolysis mode and peak power densities were predicted to increase by ca. 1.93 in fuel cell mode. This was due to increased ionic current path length along the pillars, increasing ohmic potential losses relative to faradaic impedances; as expected, such predictions depend strongly on electrode kinetic parameter values. After sintering the porous Ni(O)-YSZ pillars and their subsequent reduction with H_2 to nickel, they were assumed to constitute equipotential surfaces, depending on current collector design. Predicted current densities were up to 1011 mA cm^{-2}, far greater than in solid YSZ pillars, ultimately limited by reactant or product mass transport through porous pillars of increasing height.

Nomenclature

Symbol	Definition	Units
a_v	Active surface area per unit volume	m^{-1}
A_i	Cross-sectional area of current path	m^2
D	Distance	m
d_k	Diffusional driving force	
D_i	Diffusion coefficient of species i	$m^2 s^{-1}$
e^-	Electronic charge, 1.60219×10^{-19}	C
E^{θ}_{eq}	Standard equilibrium electrode potential	V

(*continued on next column*)

(*continued*)

E_{eq}	Equilibrium electrode potential vs. reference electrode	V
F	Faraday constant, 96,485.34	$C\,mol^{-1}$
I	Current	A
J	Current density	$A\,m^{-2}$
J_L	Mass transport limited current density	$A\,m^{-2}$
j_{loc}	Local current density	$A\,m^{-2}$

(*continued on next page*)

* Corresponding author.
E-mail address: i.jang@imperial.ac.uk (I. Jang).

https://doi.org/10.1016/j.electacta.2022.140902
Received 9 March 2022; Accepted 22 July 2022
Available online 23 July 2022
0013-4686/© 2022 The Author(s). Published by Elsevier Ltd. This is an open access article under the CC BY-NC-ND license (http://creativecommons.org/licenses/by-nc-nd/4.0/).

(*continued*)

j_o	Exchange current density	$A\,m^{-2}$
j_v	Volumetric current density $= j_{loc} \times a_v$	$A\,m^{-3}$
J_i	Mass flux density rate of species i	$g\,m^{-2}s^{-1}$
k_B	Boltzmann Constant $1.3806504 \times 10^{-23}$	$J\,K^{-1}$
M_i	Molar mass of substance i	$g\,mol^{-1}$
Nav	Avogadro's constant, 6.0220510^{23}	mol^{-1}
N	Normal vector	1
p_i	Partial pressure of gas i	Pa
p_A	Pressure	Pa
$p^0{}_i$	Partial pressure of gas under standard conditions	Pa
R	Gas constant, 8.31441	$J\,mol^{-1}K^{-1}$
R_i	Consumption of production rate of species i	$g\,m^{-3}s^{-1}$
T	Absolute temperature	K
U	Gas velocity	$m\,s^{-1}$
U	Cell potential difference	V
X_k	Mole fraction of species k	1
z_i	Number of elementary charges on species i	1
α_a	Transfer coefficient for anodic reaction	1
α_c	Transfer coefficient for cathodic reaction	1
ε	Voidage	1
ϕ	Electrical potential	V
ϕ_e	Electrical potential of electronically-conducting phase	
ϕ_i	Electrical potential of ionically-conducting phase	
η	$Overpotential = \phi_e - \phi_i - E_{eq}$	V
k_g	Permeability	m^2
μ	Dynamic viscosity	$N\,m^{-2}s$
v_i	Stoichiometric factor for species i	1
v_e	Electron stoichiometric factor	1
ρ	Density	$g\,m^{-3}$
$\sigma_{i,T}$	Conductivity of phase i at temperature T	$S\,m^{-1}$
$\overline{wi}$	Mass fraction of species i	1
$\overline{w}_k$	Mass fraction of species k	1
Δp	Pressure differential	$Pa\,m^{-1}$
Subscripts		
N	Negative electrode	
P	Positive electrode	

1. Introduction

As countries decarbonise their electrical power, steel, cement and other industries, demands are increasing for carbon-free fuels such as hydrogen [1]. Solid oxide electrochemical reactors (SOERs) are amongst the most promising gas conversion systems, enabling clean hydrogen production from steam, without CO_2 emissions when powered by renewable energy, with the highest conversion efficiencies due to their high operating temperatures [2,3].

For the development of higher performance SOERs to generate hydrogen more efficiently and economically, it is crucial to increase specific rates of electrode reactions, which occur at triple-phase boundaries (TPBs) between the electronic conductors of positive (p) and negative (n) electrodes | ionic conductors (i) | pores in the porous electrodes for transport of gaseous (g) reactants and products [4,5]. Hence, increasing TPB densities increases specific reaction rates [6], so enhancing SOER performances for the reactions (1) and (2) at positive (p) and negative (n) electrodes:

$$O_2(g) + 4e^-_{(p)} \leftrightarrow 2O^{2-}_{(i)} \quad (1)$$

$$2H_2O(g) + 4e^-_{(n)} \leftrightarrow 2H_2(g) + 2O^{2-}_{(i)} \quad (2)$$

Increased TPB densities have been reported [7–10] to be achievable by various techniques, including fabrication of micrometre scale three-dimensional (3D) ceramic structures by inkjet printing, which is also able to produce structures reproducibly, unlike conventional fabrication methods [11–13]. The method can also increase cost-effectiveness, by enabling mass production in an assembly line process [14,15].

Figs. 1 and 2 show schematics of cells with 3D structural layer components, which can be printed by inkjet printing. Fig. 1 shows a cell with a 3D structured YSZ electrolyte layer, and Fig. 2 shows porous 3D structured Ni(O)-YSZ negative electrode functional layers with 2 types of shapes. As reported in Section 4.4, the structure in Fig. 2 was predicted to increase reactor performance even more than that in Fig. 1.

However, fabricating increasingly taller YSZ pillars will not lead directly to further enhancement of SOER performance. Due to YSZ's relatively low, temperature-dependent oxygen ion conductivity and increasing ion conduction path lengths causing ohmic potential drops through such pillars, there is a saturation of performance enhancement. Hence, it is important to determine the optimal pillar geometry that produces the greatest performance, which could be normalised with respect to pillar height to optimise material utilization in fabricating such 3D structures.

In the case of Ni(O)-YSZ pillars, electrode | electrolyte interfacial areas increase with pillar height and decrease with pillar radius, so reactor performance might be expected to do likewise, subject to possible gas phase mass transport limitations. Hence, prediction of optimal pillar geometries for the whole range of kinetic to transport control would enable focusing of printing and subsequent experiments on those geometries.

Herein, we report predictions of the effects of electrode | electrolyte geometric structures on the electrochemical performance of the cell predicted by finite element modelling with COMSOL Multiphysics® software, using kinetic parameter values from the literature. The first model of cells designed with a solid YSZ pillar(s) (Fig. 1), was modelled with pillar heights of 10–150 μm and pillar diameters of 5–50 μm; the second model cell, designed with a porous Ni(O)-YSZ pillar(s) (Fig. 2), was modelled with heights of 10–190 μm and diameters of 5–30 μm. Preliminary experimental validation of the model predictions used inkjet printing of YSZ pillar structures and electrochemical analysis of their effects on reactor performances. The objective of the modelling was to estimate up-scaling factors predicted to be achievable by

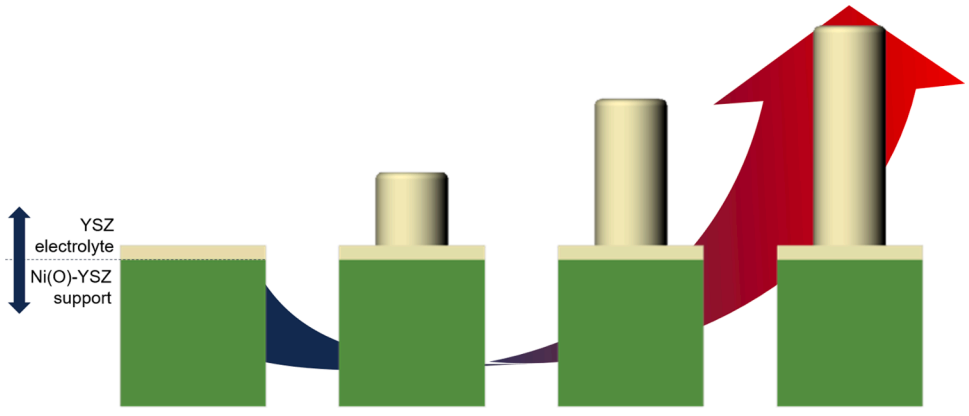

Fig. 1. Schematic of solid oxide electrolyser reactors with pillared electrolyte structures.

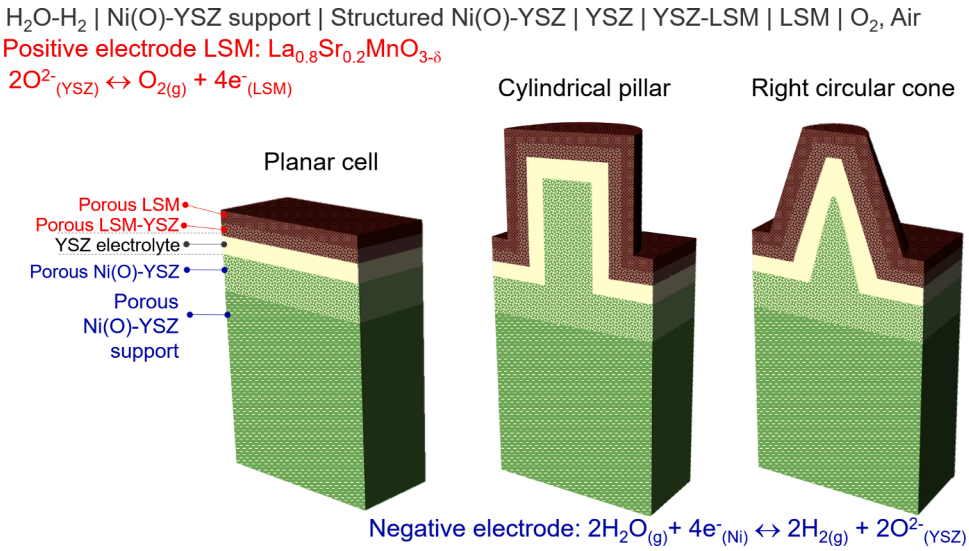

Fig. 2. Schematic solid oxide electrolyser with pillared electrolyte | negative electrode interfaces.

structuring electrode | electrolyte interfaces over the range of practically possible geometries, relative to their planar counterparts. Subsequent experiments provided preliminary validations of those predictions.

2. Experimental Methods

2.1. Solid oxide electrochemical reactor fabrication

2.1.1. Ni(O)-YSZ electrode support preparation

Ni(O)-YSZ negative electrode support layer was fabricated by pelletisation. NiO (NiO-S, Fuelcellmaterials, USA) and YSZ particles (YSZ8-U5, Fuelcellmaterials, USA) were prepared with 55 to 45 wt ratio and 10 wt% graphite was added as a pore former. The three particulate phases were ball-milled in ethanol using zirconia balls for 24 h, the dispersion was dried at 70 °C overnight and the dried powder was ground lightly, prior to being pressed at 10 MPa pressure in a 25 mm diameter pellet die. The pellet was then heat-treated firstly at 450 °C for 1 h, then at 900 °C for 5 h.

2.1.2. YSZ ink formulation

With several trivial changes, YSZ inks were prepared as published previously [12]. Firstly, YSZ particles (8YSZ-U5, Fuelcellmaterials, USA) were dispersed in de-ionized water, then dispersant (Dispex A40, Ciba-BASF, UK) was added at a concentration corresponding to 0.2 mg m^{-2} of surface area of YSZ particles. The dispersion was ball-milled with zirconia balls to break particulate agglomerates over 48 h; then the dispersion was treated witha sonication probe for 3 min, thrice, with 3 min rest intervals, then treated by bath ultrasonication for 10 min.

The sonicated dispersion was centrifuged at 1450 rpm for 2 min and 1000 rpm for 5 min to remove the particle agglomerates and to obtain a narrower particle size distribution. YSZ sediments formed after centrifuging were removed, and the YSZ ink was filtered using a 800 nm syringe filter, to remove particles larger than 800 nm, which otherwise would have caused blockage of nozzles during inkjet printing. Binder (PEG-35,000) was added at a concentration of 25 mg cm^{-3} of the total ink volume; the dispersion was stirred for another 24 h and then Natsurf 265 (Croda Chemicals, UK) was added at a concentration of 0.2 mg cm^{-3} of the total ink volume as a final step, just before printing.

2.1.3. YSZ pillar fabrication

YSZ pillars were printed on top of the YSZ electrolyte layer, coated on the surface of NiO-YSZ electrode support layer by dip-coating [16]. A 40 × 40 array of YSZ pillars with 100 μm diameter (& 80 μm) and 200 μm spacing was printed at a print speed of 42 mm s^{-1} (equivalent to 2500 Hz pulse rate) using a 3D inkjet printer (CeraDrop X-Serie piezoelectric drop-on-demand inkjet printer, Ceradrop, France) with a Samba printhead (Samba G3L, Fujifilm, Japan). The pillar arrays were printed with 100 layers to obtain the required pillar heights, with pausing and purging steps added every 10 layers to prevent nozzle blockage.

Firstly, printed pillars were heat treated at 450 °C for 1 h, then with a 5 °C min^{-1} ramp rate, at 600 °C for 2 h, to remove organic adsorbates remaining in the printed pillar structures. The printed YSZ pillared half-cells were sintered at 1400 °C for 5 h with the same ramp rate and intermediate heating step as in the pre-heat treatment. After sintering, a LSM layer was brush coated on the surface of the YSZ pillar structured electrolyte and dried on a hot plate at 80 °C, followed by sintering at 1000 °C for 2 h using a tube furnace (EHA 12/450B, Carbolite-Gero, UK), with the same ramp rate and intermediate heating step as for the pre-heat treatment procedure. For performance comparison, the same fabrication process as that for the pillared cell, though without YSZ pillar printing, was used to produce a cell with planar YSZ geometry (Fig. 1).

2.2. Analysis

2.2.1. Electrochemical Analysis

Ceramic sealant (Adhesive 668, Aremco, USA) was used to seal the Ni(O)-YSZ negative electrode side of fabricated cells on the end of a 25 mm diameter alumina tube, in which hydrogen gas or steam was flowing. Details of the current collection, sealing and reactor assembly were as reported previously [12]. NiO was reduced to Ni using a hydrogen and argon gas mixture with a ratio of 1 to 9, for 12 h at 650 °C.

Electrochemical experiments were conducted at 700 °C, 750 °C and 800 °C in a vertical tube furnace (TS1 12/60/300, Carbolite-gero, UK) with the cell at its centre. A combination of silver mesh (Alfa-Aesar, USA) and silver paste was used as current collector for the ca. 19 μm thick LSM electrode, and NiO paste for the Ni-YSZ electrode, attached to Pt wires (Goodfellow, UK) connecting the cell to an Autolab potentiostat (PGSTAT302N, Ecochemie, Metrohm, The Netherlands), used to measure its impedance and current-potential difference performance in (steam) electrolyser and (H_2-O_2) fuel cell modes. Electrochemical impedance spectroscopy (EIS) was conducted under open circuit potential conditions with 10 mV RMS amplitude and frequency range of 10^5–0.1 Hz.

2.2.2. Microstructural characterisation

An optical microscope (GXM-L3230, GT vision, UK) and camera

(GXCAM-U3PRO, GT vision, UK) were used to image the YSZ pillar structures after printing. A scanning electron microscope (SEM, JSM6400, JEOL, Japan) with 15–20 kV accelerating voltage and 15 mm working distance, was used to obtain cross-sectional images of cells and for characterisation of printed YSZ pillar structures, the surfaces of which previously had been rendered electronically conducting by gold sputtering for 40 seconds.

3. Model development

3.1. Designing models in COMSOL multiphysics®

A finite element model was built in COMSOL Multiphysics® software to represent a typical single pillar under average conditions of 50 H_2: 50 $H_2O_{(g)}$, the simplification enabling prediction of the effects of multiple physical and material parameters, of cell potential differences on current densities, and on power densities for fuel cell mode. Having defined ranges of near optimal geometries for single pillared structures, a future publication [17] will extend these results to those of models for micro-structured cells with a rectangular array of either solid electrolyte or porous electrode pillars.

Using a 3D design module in COMSOL Multiphysics® version 5.6 finite element software, two types of pillar structures were designed, firstly with YSZ pillars, as shown schematically in Fig. 1, and secondly with Ni(O)-YSZ pillars as in Fig. 2. The cylinder shape geometry tool was used to construct model YSZ pillars with diameters from 5 to 50 μm, and heights from 10 to 150 μm, with a constant 5 μm thick LSM layer structure. The cone shape geometry tool was used to construct model right circular Ni(O)-YSZ cones of diameters from 5 to 30 μm, and heights from 10 to 190 μm, with a constant 5 μm thick LSM layer, then a YSZ layer 7 μm thick with a top radius of the cone of 0.5 μm. Spacing between the centres of pillars or cones was 63 μm in both models. The COMSOL Fuel Cell and Electrolyser module was used to simulate gas transport through the model cell structures, and for calculation of their tertiary potential, current and gas compositional distributions, as functions of cell potential differences.

Table 1
Values of parameters input to models.

Parameter	Values	Units	Refs.
Spacing between pillars	63	μm	
LSM layer thickness	5	μm	
YSZ electrolyte layer thickness	7	μm	
YSZ-Ni negative electrode functional layer	10	μm	
YSZ-Ni negative electrode support thickness	100	μm	
Thickness of hydrogen gas diffusion area	150	μm	
Thickness of air gas diffusion area	200	μm	
ΔE_{eq} potential difference	1.1065	V	
Anodic exchange current density	0.01	A cm^{-2}	
Cathodic exchange current density	0.00148	A cm^{-2}	[18]
YSZ conductivity (800 °C)	4.478	S m^{-1}	[19]
Ni(O) conductivity (800 °C)	2×10^6	S m^{-1}	[13]
LSM conductivity (800 °C)	18 060	S m^{-1}	[20]
Cathodic transfer coefficient for hydrogen electrode	0.5	-	[21]
Anodic transfer coefficient for hydrogen electrode	0.5	-	[21]
Cathodic transfer coefficient for oxygen electrode	0.906	-	[18]
Anodic transfer coefficient for oxygen electrode	1.247	-	[18]
Working temperature	1 073.2	K	
YSZ-Ni negative electrode functional layer permeability	5×10^{-15}	m^2	[22]
YSZ-Ni negative electrode support permeability	5×10^{-14}	m^2	[22]
Positive electrode specific surface area value	3.9×10^7	m^{-1}	[23]
YSZ-Ni negative electrode functional layer specific surface area value	4.12×10^6	m^{-1}	[23]

3.2. Values of kinetic and other parameters

Electrochemical and physical parameter values used in the designed models are listed below in Table 1.

3.3. Model overview

Fig. 3 shows the models of the solid and porous pillars, with the width of the domain equal to the 63 μm spacing between centres of pillars on a rectangular array in the x-y plane. The four vertical boundaries (located in the x-z and y-z planes) are symmetry boundaries, across which no mass or charge transport was allowed, unlike flow parallel to the boundaries. This ensured that the model was representative of a typical pillar that was performing identically to its neighbours. The vertical dimension was sufficient for the cell thickness, including the pillar height, plus a margin to allow gas flow to and around the pillar. The gas flow was constrained to enter and leave the model via the square boundaries (in the x-y plane) at the top and bottom of the model.

The gas inlet/outlet boundary was implemented as a pressure boundary set to atmospheric pressure. This posed no constraint on the gas flow rate and avoided inadvertently fixing mass transport rates and hence cell current densities. The mole fractions of H_2 and H_2O were fixed at this boundary as a 50:50 ratio, representing a pillar at which half the inlet gas had been converted in either fuel cell or electrolyser modes, as discussed in Section 3.2. The vertical flow of gas from the boundary (from the bulk gas) to the surface of the electrode represents the flow driven by the partial pressure differences due to the consumption of reactants in the porous electrode.

The outer surface of the negative electrode (Ni-YSZ) was set to be electrical ground (0 V) and the outer surface of the positive electrode (LSM-YSZ) is set to an applied potential difference of U_{cell} relative to electrical ground. Current density and power density responses were obtained by sweeping through a range of positive electrode potentials, U_{cell}.

At the negative electrode in fuel cell mode, hydrogen gas entering the porous electrode was oxidised, decreasing the hydrogen partial pressure and producing steam that flowed out of the porous electrode to the inlet/outlet boundary. Local reaction rates depend on local overpotentials and the active surface area (triple phase boundary area in each mesh cell volume, as in Table 1).

COMSOL Multiphysics® solved coupled differential equations for: mass transport (Brinkman Equations and Diffusion), electrode kinetics (pressure independent Butler-Volmer Equation), and charge transport (Ohm's Law) to determine the secondary current distribution, allowing for the effects of overpotential. The relevant equations below were extracted from the Fuel Cell & Electrolyzer Module User's Guide [www.comsol.com]. The default solvers for the Fuel Cell and Electrolyser module were used, with the following analysis options selected:

- Include gas phase diffusion at both electrodes;
- Use Darcy's Law for momentum transport at both electrodes;
- Include N_2 in the O_2 gas mixture (as per Table 1);
- Reference pressure, 0.1 MPa;
- Mixtures treated as ideal gases.

3.4. Electrode kinetics and current distribution

A pressure independent Butler-Volmer equation was used to calculate the local current density j_{loc}, with a user defined exchange current density and anodic and cathodic transfer coefficients taken from literature for the Ni-YSZ negative electrode and from the authors' own measurements [18] for the LSM-YSZ positive electrode.

$$j_{loc} = j_0 \left[exp\left(\frac{\alpha_a F \eta}{RT}\right) - exp\left(-\frac{\alpha_c F \eta}{RT}\right) \right] \quad (3)$$

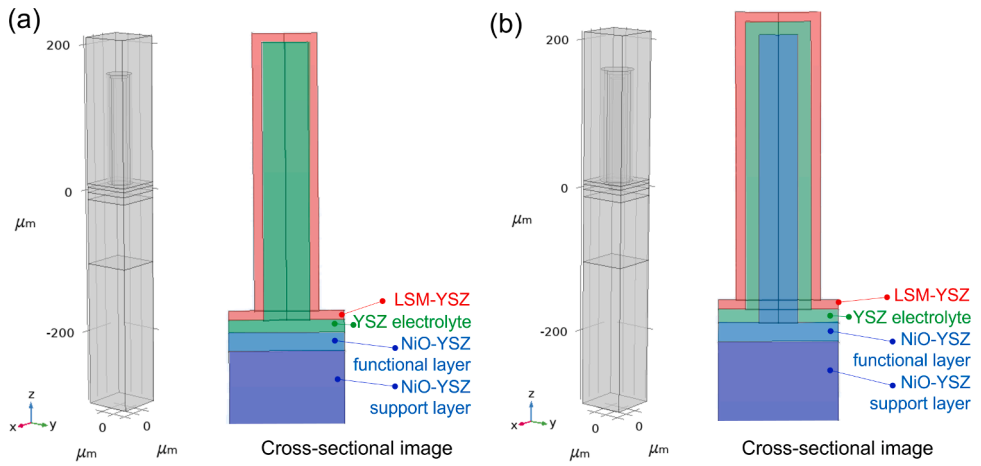

Fig. 3. Overview of COMSOL model cell geometry for (a) solid YSZ electrolyte pillar, and (b) porous Ni(O)-YSZ electrode pillar.

where α_a and α_c are the anodic and cathodic transfer coefficients and are user defined independently for the positive (LSM-YSZ) and negative (Ni(O)-YSZ) electrodes.

This approach was taken to ensure the correct relationship between the current density and overpotential from the experimentally determined behaviour of porous, micro-structured LSM-YSZ electrodes. Equilibrium potentials for positive and negative electrodes were calculated from the relevant Nernst equations:

$$E_{eq} = E^{\theta}_{eq} - \frac{RT}{{}_eF} ln \prod_i \left(\frac{p_i}{p^{\theta}_i}\right) \tag{4}$$

using reference values built-in to the COMSOL Fuel Cell and Electrolyzer module and verified by independent calculation; subscript i denotes reacting species.

The total volumetric current density j_v in a mesh element is given by a local current density j_{loc} multiplied by the active surface area per unit volume, a_v (m^{-1}). COMSOL integrates the current across the mesh elements to obtain an overall current and current density for the model.

$$j_v = j_{loc} a_v \tag{5}$$

Overpotentials for electrode reactions were calculated from:

$$\eta = \phi_e - \phi_i - E_{eq} \tag{6}$$

Where ϕ_e and ϕ_i represent the potentials in electronically- and ionically-conducting phases, respectively. The fixed boundary conditions were $\phi_{e,n} = 0$ at the surface of the negative electrode (treated as electrical ground) and $\phi_{e,p} = U_{cell}$ at the surface of the positive electrode.

The 3-dimensional current density distribution j in the electrode (subscript e) and electrolyte (subscript i) and the corresponding potential distributions ϕ_e and ϕ_i, were determined by applying Ohm's law in their respective electronically- and ionically-conducting phases:

$$j = -\sigma \cdot \nabla \phi \tag{7}$$

These equations were coupled to Butler-Volmer equations across electrode | electrolyte interfaces and the Brinkman equations for gas flow, and solved iteratively by the default COMSOL solvers.

At the four symmetry boundaries in the x-z and y-z planes, an insulation condition was set so no current flowed across those boundaries:

$$-n \cdot j = 0 \tag{8}$$

Where n is the normal vector to the boundary.

At higher cell potential differences, mass transport limitations due to electrode permeability(ies) also affect current densities, which ultimately become independent of local overpotentials for either electrode, resulting in transport limited current densities $j_{L,i}$ due to reaction of species i in either electrode. This was incorporated via the interaction of the gas flow models and the kinetics described by Butler-Volmer equations. In the case of 3D micro-structured electrodes, the flow of each species was computed numerically based on solving coupled equations for flow due to partial pressure gradients, as detailed below.

3.5. Mass transport

In COMSOL's Fuel Cells and Electrolyzer module, the flow of gas in the gas channel and porous electrode was described by the application of both the Brinkman Equations node and the Transport of Concentrated Species node (Maxwell-Stefan equations for inter-diffusion of H_2 and H_2O). In the open gas channel, the Brinkman Equations reduce to the Navier-Stokes equations, and in the porous electrodes they approach Darcy's Law. For the computation of flow in the porous electrodes, a range of graded permeabilities were applied (Table 1). The negative electrode support was highly porous, so was given a large permeability, allowing relatively unrestricted gas flow to and from its functional layer. The functional layers close to the electrolyte were fabricated from precursors with a smaller particle size, increasing active surface areas but decreasing permeabilities. Hence, as described in the Results section, a lower permeability value was used for the active layers of ca. 10 μm, enabling higher current densities before the onset of mass transport control.

Gas velocities u in the porous electrode were related to the pressure differential, ∇p, by Darcy' Law:

$$u = -\frac{\kappa_g}{\mu} \nabla p \tag{9}$$

Where κ_g is the permeability and μ is the dynamic viscosity.

The following boundary condition at the symmetry boundaries precludes gas flow across the boundaries:

$$-n \cdot \rho u = 0 \tag{10}$$

In the porous electrode, a form of the continuity equation relates the velocity of species i to a mass flux rate J_i (relative to the mass averaged velocity) and a consumption or production rate per unit volume R_i:

$$\nabla \cdot J_i + \rho(\nabla \cdot u)\omega_i = R_i \tag{11}$$

The reaction rate R_i couples the flow in the porous electrode to the kinetics via:

$$R_i = -\frac{M_i \nu_i j_v}{{}_eF} \tag{12}$$

Where j_v is the volumetric current density (A cm^{-3}) in the mesh element (Eq. (5)), ν_i is the stoichiometric coefficient for reaction of

species i and M_i is the molar mass (g mol^{-1}) of the species i.

The mass flux vector J_i is given by the Maxwell-Stefan diffusion model for concentrated species, here for constant temperature:

$$J_i = -\rho\omega_i \sum_{k=1}^{Q} \widetilde{D_{ik}} d_k \tag{13}$$

Where D_{ik} are multi-component Fick diffusion coefficients (COMSOL defaults used), d_k is the diffusional driving force, and ω_i is the mass fraction.

The diffusional driving force d_k is given by

$$d_k = \nabla x_k + \frac{1}{p_A}[(x_k - \omega_k)\nabla p_A] \tag{14}$$

The absolute pressure is p_A and x_k and ω_k are the molar and mass fractions of species k.

At the symmetry boundaries, the following condition was applied to ensure no mass flux across the boundary:

$$-n \cdot J_i = 0 \tag{15}$$

4. Results of COMSOL Simulations

4.1. YSZ pillar structures

Performance predictions of fuel cells and electrolysers with pillared structures are presented in Fig. 4, together with corresponding data for planar structures. Fig. 4a shows predicted effects on model SOFCs with YSZ pillars of current density on potential difference and power densities, for pillar heights from 10 μm to 150 μm, with diameter of 25 μm and spacing between the pillars of 63 μm. Fig. 4b shows more clearly that peak power density values increased from 247 mW cm^{-2} for the planar cell by 93% to a limiting value of 477 mW cm^{-2} for pillared cells, with values increasing by only ca. 5% for pillar heights greater than 60 μm.

Fig. 4 c and d show model predictions of the effect of pillar height on electrolyser potential difference – current density data for pillars of 25 μm diameter and 63 μm inter-pillar spacing, within the range of geometries printable with the Ceradrop X-serie 3D printer. At the thermoneutral potential of ca. 1.29 V for steam splitting at 800 °C [24,25], predicted global current densities of 391 mA cm^{-2} for a planar structure increased with pillar height for pillared structures to 446 mA cm^{-2}. In electrolyser mode, as for fuel cell mode, current densities reached a limiting value with increased pillar height, but in the former case, the upscaling factor was limited to 1.13 at heights of ca. 40 μm, above which current densities increased by only 1%.

Fig. 5 shows model predictions of the effects of current density and YSZ pillar diameter (5–50 μm) on fuel cell and electrolyser potential difference, with pillar height and inter-pillar spacing fixed at 90 μm and 63 μm, respectively; conventionally, current density is plotted on the x axis. Fig. 5a shows calculated SOFC peak power densities, which increased from 247 mW cm^{-2} for planar YSZ electrolyte to 704 mW cm^{-2} for 50 μm high YSZ pillars, an enhancement factor of 2.85. Corresponding model predictions for electrolyser mode are shown in Fig. 5b; at the thermoneutral potential of 1.29 V, current densities increased from 391 mA cm^{-2} for planar structures to 483 mA cm^{-2} for 50 μm diameter pillars of 90 μm height.

Fig. 5 shows that up to at least 50 μm, peak power densities still increased almost linearly with pillar diameter. Further studies to identify the optimum pillar diameter are required. This may in turn mean that a taller or shorter pillar than 90 μm becomes optimal, which also will depend on the kinetic parameter values and micro-structure of the porous electrode, so is unlikely to be optimal for different fabrication techniques, particle size etc.

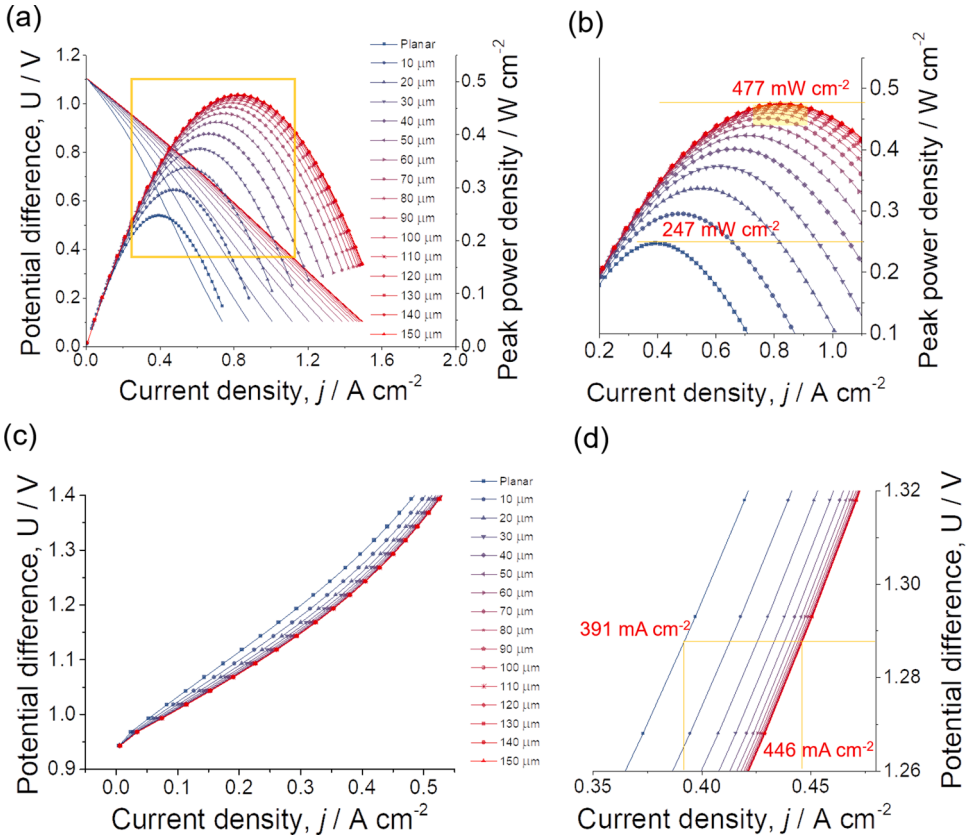

Fig. 4. Model-predicted effects of current density and YSZ pillar height on potential difference (a, b) in fuel cell mode with 3% H_2O, and (c-d) in electrolysis mode with 50% H_2O; YSZ pillar diameter 25 μm and inter-pillar spacing 63 μm.

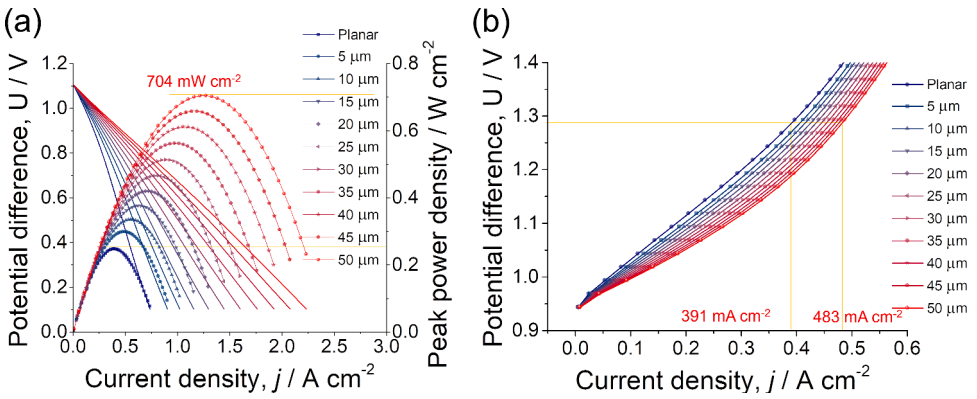

Fig. 5. Model-predicted effects of current density and YSZ pillar diameter on potential difference (a) and power densities with 3% H_2O in fuel cell mode; (b) in electrolysis mode with 50% H_2O; pillar height 90 µm and inter-pillar spacing 63 µm.

4.2. Ni(O)-YSZ pillar structures

As shown in Fig. 2, model Ni(O)-YSZ cylindrical pillars and right circular cones were designed, and their predicted performance compared with that of the corresponding planar cell. Right circular cones have higher surficial area to volume ratios compared to cylindrical pillars, transport between which could become limiting for tall pillars with narrow inter-pillar gaps.

Fig. 6 shows model performance predictions for fuel cells and electrolysers with cylindrical pillared Ni(O)-YSZ functional layers. Increasing their height in SOFC mode increased peak power densities by a factor of 4.9 (Fig. 6a), which was much greater than for YSZ pillars (Fig. 4) in which ohmic potential losses were significant, unlike (assumed) in Ni(O)-YSZ pillars. However, peak power densities did not increase linearly with pillar height, with the increase of peak power densities decreasing from 26.5% increase per 10 µm height to 20.5%, as pillar heights were increased notionally from 0 to 200 µm. Nevertheless, there is potential for much taller pillars before the incremental improvements become marginal.

In electrolysis mode, the lack of linearity with increasing pillar height was more evident, leading to limiting behaviour as shown in Fig. 6b for pillar heights of ca. 150–170 µm., This was due to limitations in steam transport rates through the pillar structure. At the thermoneutral potential difference of 1.29 V for steam electrolysis, current densities increased from 391 mA cm^{-2} for planar structures to that limiting value of 1011 mA cm^{-2} for pillars 190 µm high.

When pillar diameters were notionally increased from 5 µm to 30 µm at a constant 90 µm pillar height, current densities increased almost proportionally with the increase of the surficial area value (Fig. 6c and d). In a pillar array, electrode | electrolyte areas could be increased by decreasing pillar diameter and decreasing inter-pillar spacing between pillars, potentially thereby increasing reactor performance per unit volume. However, smaller pillar diameters exhibited significant gas transport limitations (5 µm diameter pillar in Fig. S1 a and b), thereby

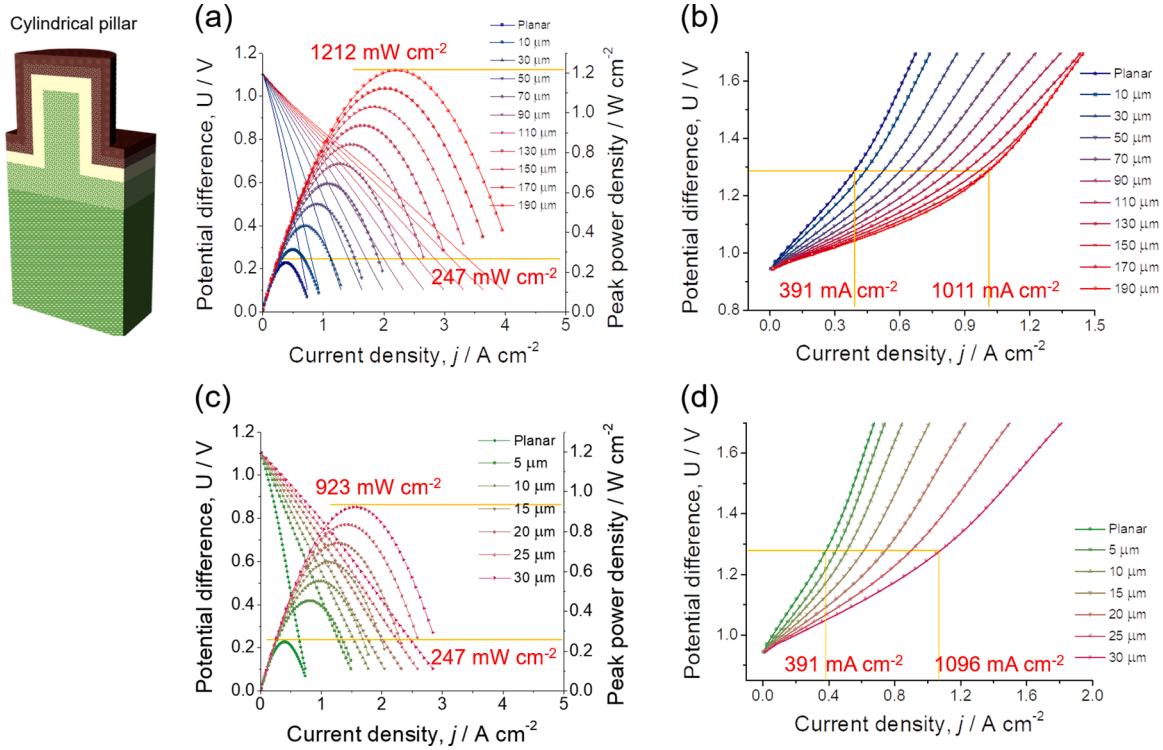

Fig. 6. Predicted effects of current density on potential differences for fuel cells and electrolysers with cylindrical Ni(O)-YSZ pillared functional layers; (a, b) for variable pillar height (10–190 µm) and 20 µm pillar diameter; (c, d) for variable pillar diameter (5–30 µm) and 90 µm pillar height.

limiting reactor performance. This effect was due to a pillar's area / volume ratio ≈ 4 / d_p for tall, thin pillars, so with decreasing diameter (d_p), electrode reaction has a greater tendency to deplete gaseous reactant diffusing through its porous cross section. Hence, optimisation of pillar geometries is required, using COMSOL simulations to optimise active areas and reactor performance, prior to the printing.

For steam reduction to hydrogen, Fig. 7 shows predicted spatial distributions of H_2O mole fractions and of local current densities in a Ni-YSZ porous pillar 150 μm high and 20 μm in diameter. For the thermoneutral potential difference (1.29 V), Fig. 7(a) predicted that steam was depleted progressively with increasing pillar height, the mole fraction of H_2O decreasing by half at the pillar height of 150 μm. The corresponding distribution of local current densities in Fig. 7 (c) was relatively homogeneous with increasing height. For a potential difference of 1.7 V, Fig. 7(b) predicts progressive depletion of steam with increasing pillar height, but unlike at the thermoneutral potential difference, leading to total depletion and hence zero current density (Fig. 7 (d)) at the top part of the pillar, unlike in Fig. 7(c).

These results explain the global performance saturation with increasing pillar height, as shown in Fig. 6(b). Hence, pillar heights need to be optimised, depending on (predicted) current density distributions which in turn depend on operating potential differences.

Fig. 8 shows model predictions for fuel cells and electrolysers with right circular cone structures, which as expected in electrolysis mode, did not exhibit significant performance limitations (Fig. 8b), due to the spatial distribution of the density of reaction sites and of local mass

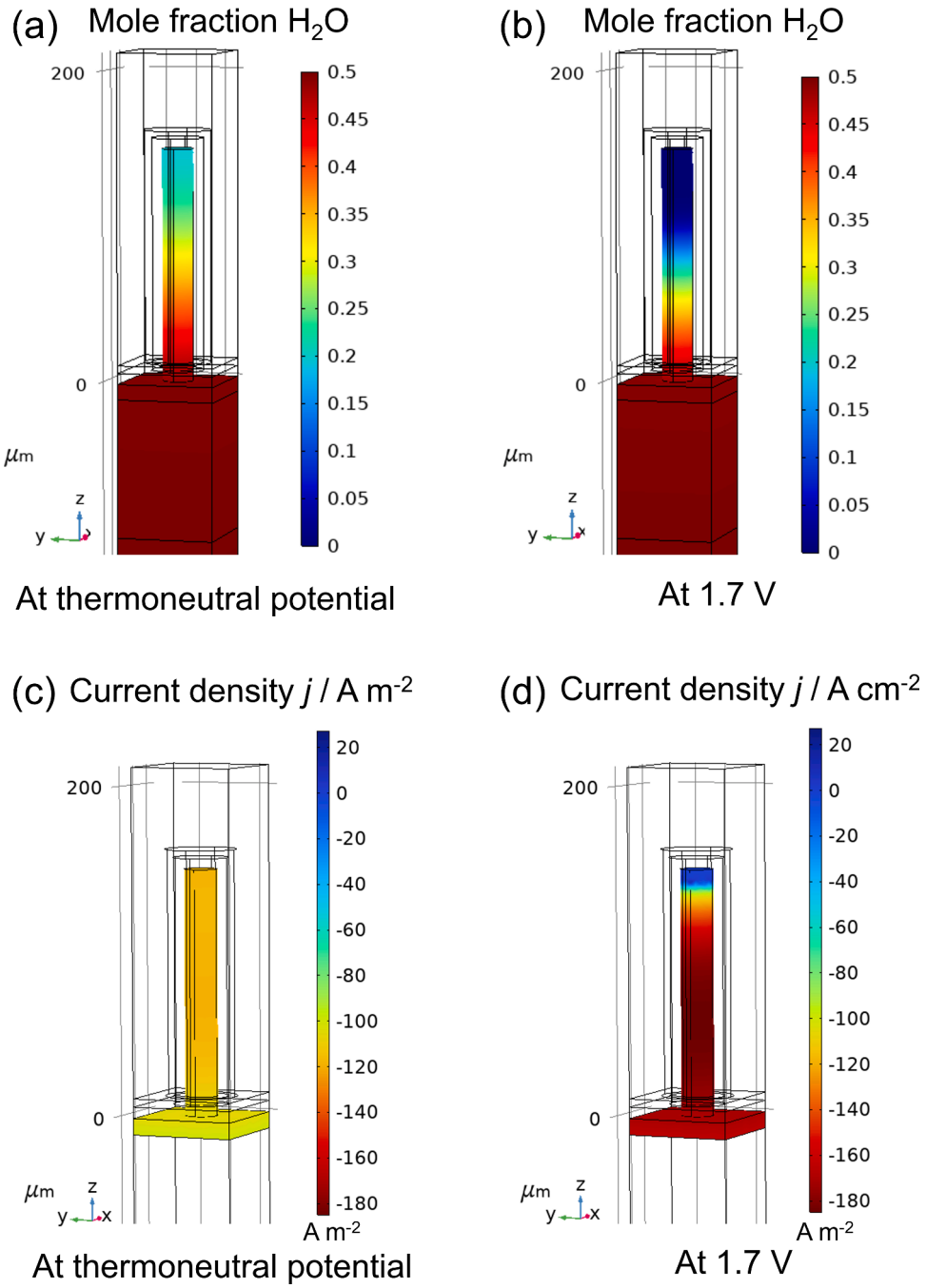

Fig. 7. Predicted spatial distributions, due to $H_2O(g) + 2e^-_{(n)} \rightarrow H_2(g) + O^{2-}_{(i)}$ in porous Ni-YSZ pillar, of: H_2O mole fractions at (a) thermoneutral potential difference (1.29 V), (b) 1.7 V; local current densities at: (c) thermoneutral potential difference (1.29 V), (d) 1.7 V.

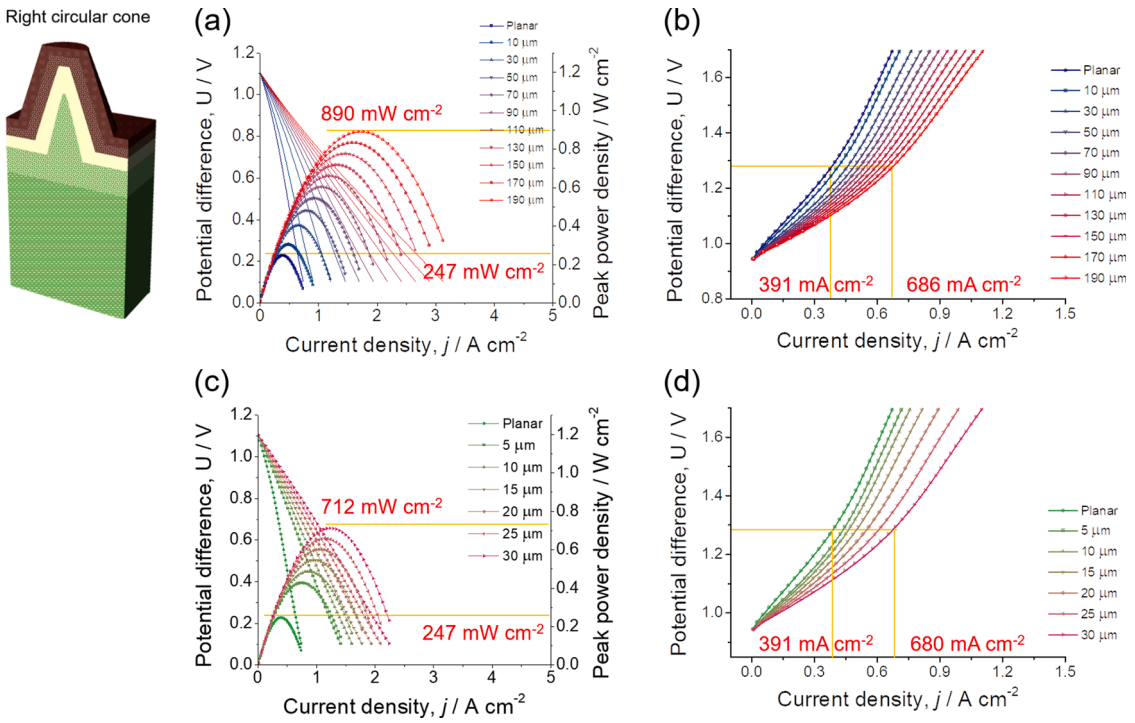

Fig. 8. Model-predicted effect of current density on potential differences of fuel cells and electrolysers with right circular cone shaped Ni(O)-YSZ negative electrodes, (a, b) with increasing cone height (10– 190 µm) and constant 20 µm diameter; (c, d) increasing cone diameter (5–30 µm) and constant 90 µm height.

transport rates with height, unlike those of cylindrical pillar structures (Fig. S2). In fuel cell mode, peak power densities were predicted to increase a factor of 3.6, when the height was increased from 10 µm to 190 µm, and by a factor of 2.9, when the diameter was increased from 5 to 30. In electrolysis mode at the thermoneutral potential difference of 1.29 V for steam splitting, current densities increased by a factor of 1.75 when the pillar height was increased from 10 µm to 190 µm, and by a factor of 1.74 when the diameter was increased from 5 µm to 30 µm. The global performance was less than for corresponding cylindrical pillar cells, but the greater surficial area to volume ratio of cones may lead to greater material utilisation, as shown in Table 2. With right circular cone shaped structures in SOFCs, peak power densities of 3D structured Ni(O)-YSZ functional layer volume ratio was higher than for corresponding cylindrical pillar cells. This could be explained by the higher surface area to volume ratio of the right circular cone shape, demonstrating effective material utilisation for pillar construction.

Additionally, cones may be easier to over-print with defect-free electrolyte and second electrode materials than cylindrical pillars, with their sharp edges that may result in sloughing of such overlayers, though the feasibility has yet to be established of 3D printing cone-shaped structures with base diameters of 10 s µm.

The effects of other factors that affect reactor performance are shown in Figs. S1 and S3 in the supplementary information. In Fig. S1a and b, the model-predicted effects of current density and pillar height on fuel cell and electrolyser potential differences is reported for 5 µm diameter Ni(O)-YSZ pillars with a permeability of 5×10^{-15} m^2. The effect of decreasing the pillar diameter from 20 µm was to decrease the dependence of peak power densities per 10 µm height to 24% of the amount for the first 10 µm height. In electrolysis mode, predicted current densities at 1.29 V reached limiting values at ca. 130 µm pillar height, exhibiting $<$ 10% increase compared to the increase for the first 10 µm.

As expected, the permeability of the Ni(O)-YSZ negative electrode functional layer also greatly affected transport limited reactor performances. Fig. S1c and d shows results of the simulation for Ni(O)-YSZ pillars with a lower gas permeability (10^{-15} m^2), resulting in greater current density limitations with pillar height. Hence, fabricating Ni(O)-YSZ functional layers with adequate gas permeability is crucial to achieving required reactor performance.

From Fig. S3 in the Supplementary Information, when the water vapour content of the gas in the negative electrode was decreased to 20%, current densities at 1.29 V limited with pillar heights of 110–130 µm (Fig. S3b), a significant decrease compared with 50% water vapour (Fig. S3a). As expected, transport limited current densities depend on both reactant concentration and the permeability of the functional layer structure, which varies with particle size, pore former concentration and size, etc., and so control (mean) mass transport rate coefficients.

COMSOL simulation results for Ni(O)-YSZ pillar structures demonstrated the need to optimise their diameter and height, not merely electrolyte | negative electrode interfacial areas, prior to printing 3D microstructures, sintering and costly experimental validation, to

Table 2
Ratios of peak power density to Ni(O)-YSZ functional layer volume (including pillar and planar functional layer below the pillar) in each cylindrical pillar and right circular cone models, and their surface area to volume ratios (excluding volume of planar AFL layer below the pillar and bottom surface of pillar structures).

	Cylindrical pillar	Right circular cone		
Height / µm	Peak power density / Volume * 10^5 / W cm^{-5}	Surface area / Volume * 10^{-2} / cm^{-1}	Peak power density / Volume * 10^5 / W cm^{-5}	Surface area / Volume * 10^{-2}/ cm^{-1}
0 (Planar)	6.22	-	6.22	-
10	7.28	30.00	7.49	42.43
30	8.78	23.33	9.41	31.62
50	9.75	22.00	10.66	30.59
70	10.46	21.43	11.55	30.30
90	10.86	21.11	12.34	30.18
110	11.30	20.91	12.95	30.12
130	11.59	20.77	13.45	30.09
150	11.83	20.67	13.92	30.07
170	12.04	20.59	14.40	30.05
190	12.20	20.53	14.94	30.04

optimise fuel cell or electrolyser performance.

5. Experimental validation

For experimental validation of the effect of YSZ pillar structures on the enhancement of fuel cell and electrolyser performance, firstly pillars were inkjet printed on planar YSZ layers that had been dip-coated onto the Ni(O)-YSZ anode support layer [16]. Fig. S4 shows optical microscopy images, of as-printed pillar arrays and structures – prior to sintering – with 80 μm and 200 μm inter-pillar distances. Fig. S4a shows an optical image of the entire 40 by 40 array of YSZ pillars before sintering; the well-printed pillar structures are shown in more detailed optical images in Fig. S4b–e at low magnification (b and c), and higher magnification (d and e). Images in Fig. S4c and d were illuminated from the side to give a three-dimensional effect, which was less apparent under vertical illumination, as shown in Fig. S4b and c.

Fig. 9 shows images of pillar structures after sintering. From the top view image of the pillars in the upper row of Fig. 9a–c, the diameter of pillar decreased to ca. 60 μm from 80 μm, corresponding to a shrinkage ratio of ca. 25%. Fig. S5 provides a more accurate comparison of pillar images before and after sintering.

The cross-sectional images in the bottom row Fig. 9d–f confirmed that the sintered YSZ pillars of ca. 90 μm height, had robust structures and were well-attached to the surface of the planar YSZ layer. The pillars were printed with 100 layers, pillar height depending on the number of printed layers and the particle concentration of the printing ink used, as described in more detail below.

Fig. 10a and b reports the effects of current density on potential differences and power densities of fuel cells with and without pillar structures, the former exhibiting ca. 56% enhanced peak power density value at 800 °C operating temperature, in qualitative agreement with COMSOL predictions for YSZ pillar cells shown in Fig. 4. However, both cells exhibited peak power densities < 100 mW cm^{-2}, significantly less than reported in the literature for similar cells with an electrolyte layer thickness of > 10 μm, as shown in Fig. 10 c and d. It is noted that the positive electrode was composed of LSM alone, with decreased density of triple phase boundaries than in composite LSM-YSZ positive electrodes, which may explain the overall low performance.

Printed with 80 μm diameter and 200 μm inter-pillar distance, the YSZ pillars imaged in Fig. 10c and d appeared quite depressed compared to the pillars in Fig. 9. The YSZ particulate ink used for printing the pillar structure had a particle concentration of ca. 10 wt%, whereas the ink used for printing the pillars imaged in Fig. 9 had a YSZ concentration of 18.6 wt%. The pillars were printed with the same number of layers, so the height of ca. 25 μm, lower than the expected 90 μm height seems to be due to the ink composition. The pillars are less cylindrical and more spread out. This demonstrates that particle concentrations in inks have a critical effect on pillar shape; lower concentrations result in less inorganic material in each layer, which would be thinner, resulting in the shorter pillars. Hence, the implication is that inks should have particle concentration ≥ 18 wt%. Additionally, the viscosity of the ink is one other main factor that affects the pillar shape, causing the coffee stain effect when the ink has a high viscosity, as explained in previous publication [26,27].

6. Conclusions

Finite element simulations predicted the effects of single YSZ electrolyte pillar and single Ni(O)-YSZ electrode pillar and cone structures on solid oxide fuel cell and electrolyser performances, which increased relative to their planar counterparts by a factor of up to 2.85 for YSZ pillars, and up to 4.9 in Ni(O)-YSZ pillars. More importantly, those computational predictions demonstrated that there are optimal geometries for YSZ and Ni(O)-YSZ pillar structures for optimising SOER performances, depending on physicochemical and kinetic parameter values. In electrolysis mode, with increasing pillar heights, current densities at fixed potential differences were predicted to reach limiting values, of ca. 0.44 A cm^{-2} for YSZ pillars and 1 A cm^{-2} for Ni(O)-YSZ pillars, despite taller pillars increasing electrode | electrolyte interfacial areas. With increasing diameter, porous Ni(O)-YSZ electrode pillars were predicted to allow taller pillars, enhancing current densities relative to planar counterparts. Conversely, with smaller diameter pillars, current densities were predicted to be limited to shorter pillar heights, due to their area to volume ratios causing electrode reactions close to their surfaces to deplete reacting gas as it diffuses axially though the pillar, so limiting local current densities. Cylindrical porous pillars were predicted to outperform conical pillars for a fixed geometrical area.

Accurate physicochemical and kinetic parameter values were shown to be critical to defining optimal geometric values for optimising predicted fuel cell and electrolyser performances, thereby focusing subsequent experimental cell fabrication and performance validation.

In future, YSZ and Ni(O)-YSZ pillar structures with ranges of diameters and heights will be 3D inkjet printed, followed by more extensive experimental validation of the model predictions of geometrical effects on fuel cell and electrolyser performances of the fabricated cells.

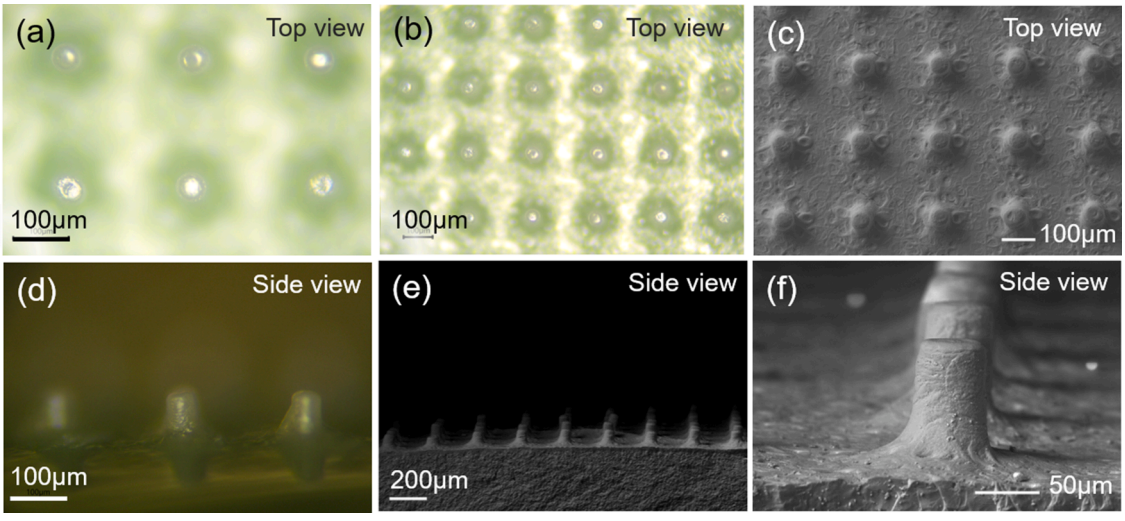

Fig. 9. Optical microscope images (a, b, d) and SEM images (c, e, f) of the top view and cross-sectional view of sintered YSZ pillars printed with 100 layers and sintered at 1400 °C for 5 h.

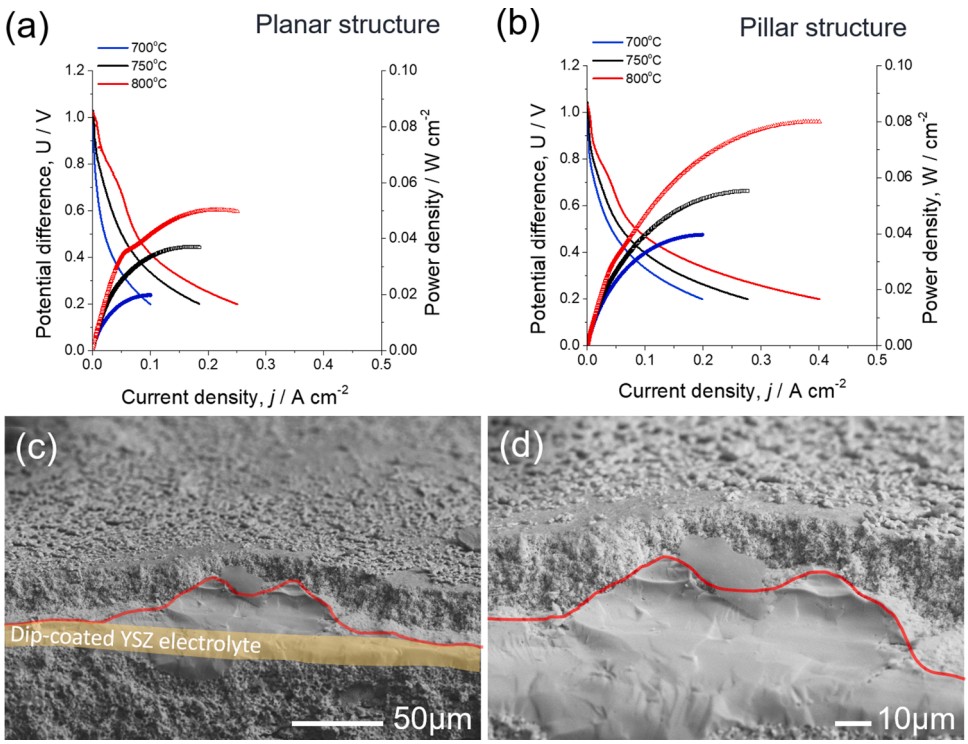

Fig. 10. Effects of current density on potential differences and power densities for: (a) planar structured SOFC, and (b) pillar structured SOFC; (c-d) SEM images of cross section of pillar structured SOFC after testing.

Declaration of Competing Interest

The authors declare that they have no known competing financial interests or personal relationships that could have appeared to influence the work reported in this paper.

Acknowledgement

The authors thank Shell Global Solutions International B.V for a research contract providing post-doctoral research associateships for I.J. and J.C.A.

Supplementary materials

Supplementary material associated with this article can be found, in the online version, at doi:10.1016/j.electacta.2022.140902.

References

[1] V. Oldenbroek, S. Wijtzes, K. Blok, A.J. van Wijk, Fuel cell electric vehicles and hydrogen balancing 100 percent renewable and integrated national transportation and energy systems, Energy Convers. Manag. 9 (2021), 100077.
[2] K. Kendall, M. Kendall, High-temperature Solid Oxide Fuel Cells For the 21st century: fundamentals, Design and Applications, Elsevier, 2015.
[3] D.J. Brett, A. Atkinson, N.P. Brandon, S.J. Skinner, Intermediate temperature solid oxide fuel cells, Chem. Soc. Rev. 37 (2008) 1568–1578.
[4] R. O'Hayre, D.M. Barnett, F.B. Prinz, The triple phase boundary: a mathematical model and experimental investigations for fuel cells, J. Electrochem. Soc. 152 (2005) A439.
[5] R.M. Ormerod, Solid oxide fuel cells, Chem. Soc. Rev. 32 (2003) 17–28.
[6] X. Deng, A. Petric, Geometrical modeling of the triple-phase-boundary in solid oxide fuel cells, J. Power Source 140 (2005) 297–303.
[7] P.A. Connor, X. Yue, C.D. Savaniu, R. Price, G. Triantafyllou, M. Cassidy, G. Kerherve, D.J. Payne, R.C. Maher, L.F. Cohen, Tailoring SOFC electrode microstructures for improved performance, Adv. Energy Mater. 8 (2018), 1800120.
[8] J.M. Vohs, R.J. Gorte, High-performance SOFC cathodes prepared by infiltration, Adv. Mater. 21 (2009) 943–956.
[9] J. An, Y.-B. Kim, J. Park, T.M. Gür, F.B. Prinz, Three-dimensional nanostructured bilayer solid oxide fuel cell with 1.3 W/cm^2 at 450 C, Nano Lett. 13 (2013) 4551–4555.
[10] M. Kishimoto, M. Lomberg, E. Ruiz-Trejo, N.P. Brandon, Enhanced triple-phase boundary density in infiltrated electrodes for solid oxide fuel cells demonstrated by high-resolution tomography, J. Power Source 266 (2014) 291–295.
[11] J. Ruiz-Morales, A. Tarancón, J. Canales-Vázquez, J. Méndez-Ramos, L. Hernández-Afonso, P. Acosta-Mora, J.M. Rueda, R. Fernández-González, Three dimensional printing of components and functional devices for energy and environmental applications, Energy Environ. Sci. 10 (2017) 846–859.
[12] N. Farandos, L. Kleiminger, T. Li, A. Hankin, G.H. Kelsall, Three-dimensional inkjet printed solid oxide electrochemical reactors. I. Yttria-stabilized zirconia electrolyte, Electrochim. Acta 213 (2016) 324–331.
[13] S. Masciandaro, M. Torrell, P. Leone, A. Tarancón, Three-dimensional printed yttria-stabilized zirconia self-supported electrolytes for solid oxide fuel cell applications, J. Eur. Ceram. Soc. 39 (2019) 9–16.
[14] N. Kostretsova, A. Pesce, M. Nuñez, A. Morata, M. Torrell, A. Tarancón, Self-supported solid oxide fuel cells by multimaterial 3D printing, ECS Trans. 103 (2021) 59.
[15] G.D. Han, K. Bae, E.H. Kang, H.J. Choi, J.H. Shim, Inkjet printing for manufacturing solid oxide fuel cells, ACS Energy Lett. 5 (2020) 1586–1592.
[16] I. Jang, C. Kim, S. Kim, H. Yoon, Fabrication of thin films on an anode support with surface modification for high-efficiency intermediate-temperature solid oxide fuel cells via a dip-coating method, Electrochim. Acta 217 (2016) 150–155.
[17] I. Jang, G.H. Kelsall, Fabrication of 3D NiO-YSZ structures for enhanced performance of solid oxide fuel cells and electrolysers, Electrochem. Commun. 137 (2022) 107260.
[18] N.M Farandos, I Jang, J.C. Alexander, G.H. Kelsall, 3-D Inkjet Printed Solid Oxide Electrochemical Reactors III. Cylindrical Pillared Electrode Microstructures, Electrochim. Acta (2022) 140834.
[19] C. Zhang, C.J. Li, G. Zhang, X.J. Ning, C.X. Li, H. Liao, C. Coddet, Ionic conductivity and its temperature dependence of atmospheric plasma-sprayed yttria stabilized zirconia electrolyte, Mater. Sci. Eng. 137 (2007) 24–30.
[20] D. Das, R.N. Basu, Improved polarization behaviour of nanostructured $La_{0.65}Sr_{0.3}MnO_3$ cathode with engineered morphology, Int. J. Hydrogen Energy 42 (2017) 15347–15358.
[21] D. Cui, C. Yang, K. Huang, F. Chen, Effects of testing configurations and cell geometries on the performance of a SOFC: a modeling approach, Int. J. Hydrog. Energy 35 (2010) 10495–10504.
[22] D. Simwonis, H. Thülen, F. Dias, A. Naoumidis, D. Stöver, Properties of Ni/YSZ porous cermets for SOFC anode substrates prepared by tape casting and coat-mix® process, J. Mater. Process. Technol. 92 (1999) 107–111.
[23] M. Kishimoto, H. Iwai, M. Saito, H. Yoshida, Quantitative evaluation of solid oxide fuel cell porous anode microstructure based on focused ion beam and scanning electron microscope technique and prediction of anode overpotentials, J. Power Source 196 (2011) 4555–4563.
[24] J.B. Hansen, Solid oxide electrolysis–a key enabling technology for sustainable energy scenarios, Faraday Discuss 182 (2015) 9–48.

[25] A. Buttler, H. Spliethoff, Current status of water electrolysis for energy storage, grid balancing and sector coupling via power-to-gas and power-to-liquids: a review, Renew. Sustain. Energy Rev. 82 (2018) 2440–2454.
[26] M. Majumder, C.S. Rendall, J.A. Eukel, J.Y. Wang, N. Behabtu, C.L. Pint, T.Y. Liu, A.W. Orbaek, F. Mirri, J. Nam, Overcoming the "coffee-stain" effect by compositional Marangoni-flow-assisted drop-drying, J. Phys. Chem. B 116 (2012) 6536–6542.
[27] A. Friederich, J.R. Binder, W. Bauer, Rheological control of the coffee stain effect for inkjet printing of ceramics, J. Am. Ceram. Soc. 96 (2013) 2093–2099.